Journal of Applied Fluid Mechanics, Vol. 18, No. 9, pp. 2282-2296, 2025.
Available online at www.jafmonline.net, ISSN 1735-3572, EISSN 1735-3645.
https://doi.org/10.47176/jafm.18.9.3408

Assessment of Erosion Wear on a Reducing Pipe in a Propulsion System Using the Eulerian-Lagrangian Method

A. Chen[1], Y. Yu[1†] and S. Xiao[2]

[1] *School of Energy and Power Engineering, Nanjing University of Science and Technology, Nanjing, Jiangsu Province, 210094, China*
[2] *Weichai Power Co., Ltd., Weifang, Shandong Province, 261061, China*

†*Corresponding Author Email: 801105ndd@njust.edu.cn*

ABSTRACT

The erosion wear on a forcing cone (FC), which is a reducing pipe structure in a barrel, is a transient complicated process that is caused by a high-speed dense propellant particle group. This process leads to the reduced propulsive performance and shortened useful life of a propulsion system. The accurate evaluation of this phenomenon is a formidable task. In this study, an effective evaluation model is developed to tackle this challenge, where the initial interior ballistic model is integrated into a computational fluid dynamics and discrete element method (CFD-DEM) coupling framework to reproduce the propellant gas source. The detailed particle interactions are factored into the model to enhance the precision. The results show that a gushing phenomenon exists when the particles move in the FC. The main interaction between the particles and the wall gradually changes from an impact interaction to a friction interaction. The erosion loss mass increases exponentially over time. Finally, the erosion distribution varies from an annular irregular distribution to a cloud-like distribution from the left side of the FC to the right side. The maximum erosion depth and the mass loss rate are positive with the FC's taper angle. When the taper is 1/5, the mass loss can reach up to 60 mg and the maximum erosion depth can reach 1.1 μm.

Article History

Received January 31, 2025
Revised April 1, 2025
Accepted April 24, 2025
Available online July 5, 2025

Keywords:

Erosion wear mechanisms
Reducing pipe structure
High-speed dense gas-solid flow
Computational fluid dynamics and discrete element method
Taper angle
Propulsion system

1. INTRODUCTION

There is a complex erosion phenomenon on the inner surface of a propulsion system that is caused by the complex high-speed gas-solid reaction flow in the combustion and propulsion process. Specifically, the forcing cone (FC) is a reducing pipe structure in the barrel. The wall of the FC is at an angle to the gas-solid flow from the chamber, which causes the inner face of the wall to be subjected to impact and friction from high-speed particles during the initial interior ballistic process (IIBP). This increases erosion damage to the FC surface, which in turn leads to adverse effects on the operation performance and limits the useful life of the propulsion system (Fu et al., 2009; Tao et al., 2010; Yang et al., 2024). Consequently, it is of great significance to analyze in depth the erosion wear behavior of an FC that is caused by propellant particles to fully assess the erosion damage risk on the inner surface of the propulsion system.

Recently, the erosion phenomenon of propulsion systems has been studied, primarily from the perspectives of erosion mechanism analysis (Chung et al., 2007; Dou et al., 2022), erosion risk evaluations (Sopok et al., 2005; Li et al., 2023b), and other aspects (Li et al., 2024; Wang et al., 2024;). Underwood et al. (2004) calculated the transient thermal damage to gun-steel material by summarizing the relationship between the thermal expansion stress and material depths and obtaining the fragment exfoliating conditions. Ewing et al. (2013) proposed a one-dimensional (1D) heat transfer interface erosion model for the inner surface of a barrel. The model accounted for factors such as heat transfer, material decomposition, permeation, diffusion, and thermochemical erosion of the pyrolysis gas in detail. Rezgui et al. (2019) found that the thermochemical erosion of gun steel was chiefly related to the thermal load, the surface characteristics, and the chemical interaction between the combustion products and the barrel surface. Li et al. (2020b) showed that erosion was an important destruction mechanism for the starting point of gun rifling and that this erosion belt expanded with the

NOMENCLATURE

ψ	percentage of the burned propellant	ε_l	volume fraction of the fluid
Z	relative thickness of the burned propellant	ρ_l	density of the fluid
χ	shape characteristic parameters of propellant	$\boldsymbol{v}_l$	velocity of the fluid
λ	shape characteristic parameters of propellant	$\boldsymbol{\tau}$	viscous stress tensor of the fluid
μ_2	shape characteristic parameters of propellant	$\boldsymbol{S}$	momentum source term
μ_1	burning-rate coefficient	k	turbulent kinetic energy.
e_1	arc thickness of propellan	μ	dynamic viscosity
P	average pressure in the chamber	γ	kinematic viscosity
α_1	residual volume of the gas	G_k	change of turbulent kinetic energy caused by the velocity gradient
ρ_p	gunpowder particle density	G_b	change of turbulent kinetic energy caused by the buoyancy
S_1	cross-sectional area of the barrel	Y_M	pulsation expansion in the compressible turbulence
m	mass of the propellant charge	m_p	mass of particles
V_0	volume of the chamber	$\boldsymbol{v}_p$	velocity of particles
φ	secondary power coefficient	$\boldsymbol{\omega}_p$	angular velocity of particles
m_1	mass of the projectile	$\boldsymbol{F}_g$	gravity force of particles
v_1	velocity of the projectile	$\boldsymbol{F}_I$	drag force
l	displacement of the projectile	$\boldsymbol{F}_c$	collision force
ρ	inertia radius of the projectile	$\boldsymbol{F}_p$	pressure gradient force
r	radius of the projectile	$\boldsymbol{R}_i^*$	vector from the particle center of mass to the contact point.
θ	rifling angle	E^*	equivalent Young's modulus
f	gunpowder force	R^*	equivalent radius
k_1	adiabatic index	S_n	normal stiffness
p_d	projectile base pressure	S_t	tangential stiffness
p_t	chamber bottom pressure	m^*	equivalent mass

increase in the number of shooting times. Zou et al. (2020) analyzed the effects of the density, thermal conductivity, and specific heat capacity of gun steel on erosion based on Fourier heat conduction theory. Chevalier et al. (2015) and Li et al. (2020a) developed a barrel erosion and life prediction model with consideration of the influence of bearing band friction on a barrel based on a simulation test and a shooting test with different caliber barrels. Wang L. et al. (2022) and Li et al. (2023a) proposed a universal surface erosion model with consideration of projectile collision wear, melting exfoliation, and high-speed jet erosion. These studies on the erosion mechanisms of the inner surface in a propulsion system were mainly focused on thermochemical erosion, gas jet erosion, and projectile mechanical wear (Lee et al., 2009; Borges et al., 2020; Yang et al., 2020;). Research on the erosion wear of an FC caused by propellant particles in an IIBP has been reported rarely, resulting in an inadequate comprehension of the erosion mechanism within a propulsion system.

Erosion wear caused by solid particles is widespread in various engineering fields, such as erosion wear on the outer surface of an aircraft caused by sand particles (Bai et al., 2020; Guo et al., 2025;), erosion wear in a turbine due to a large number of sediment particles (Chen & Tan, 2024; Dhiman et al., 2025;), and the erosion wear phenomenon on the inner surface of a pipeline during transportation (Singh et al., 2019; Perera et al., 2024;). At present, a large amount of research has been carried out on the erosion wear of a pipeline with various engineering structures, and erosion wear behaviors can be studied at the particle scale utilizing numerical simulation. Peng & Cao (2016) employed the Det Norske Veritas (DNV) erosion model to explore the erosion distribution of a 90° elbow affected by the flow velocity, particle mass flow rate, and pipe diameter. Two equations for predicting the maximum erosion location were obtained. Xie et al. (2020) analyzed the erosion behavior of tandem 90° elbows and found that the maximum erosion region always appeared at the first elbow. Based on the CFD and discrete phase model (DPM), Zhang et al. (2021) investigated the particle flow and the erosion mechanism of T-shaped, Y-shaped, and y-shaped tee tubes. It was found that the particles were more concentrated in the downstream region, the collision probability increased with confluence, and the erosion rate of the y-shaped tubes was small. Hong et al. (2023) integrated the mixture model and the erosion model through the CFD-DPM method to study the erosion behavior of the 90° elbow, right-angle pipe, and blind tee. It was found that the erosion areas of the 90° elbow and the right-angle pipe were primarily concentrated in the downstream section, while that of the blind tee was mainly concentrated in the plugged section. Wang S. et al. (2022) found that non-coplanar π-shaped pipes produced a swirling effect on fluids and particles

that affected the erosion rate of the elbows. Zolfagharnasab et al. (2021) conducted a comparative study on the erosion mechanism of square duct elbows and round pipe elbows and found that the erosion rate of the square pipe was smaller than that of the round pipe. It had less dependence on the particle size and the velocity. Wang et al. (2023) investigated the flow irreversibility and erosion of the connection of pipe resistance components with CFD-DEM and indicated that the connection position of the reducer and elbows affected the maximum erosion rate. Lin et al. (2020) found that the number of particles had an important impact on the erosion of the gate valve, and the range of the erosion gradient zone and the maximum erosion rate decreased with the increase of the particle size. The aforementioned numerical investigations concerning particle-induced erosion predominantly used the DPM and DEM methods. The DPM method ignoring the interaction between particles is suitable for the dilute gas–solid flow. The DEM method can be used to calculate the interaction between particles and is suitable for dense gas-solid flow, which is why it can be used in this work.

In the abovementioned studies, erosion wear on the outer surface of an aircraft was caused by high-speed sparse particle groups in free space. The erosion wear in pipelines was induced by low-speed sparse particle groups in a confined space. In a propulsion system, the erosion wear of the FC wall during the IIBP differs from both of these and has its own particularities. This is an erosion wear phenomenon of the reducing pipe structure that is caused by high-speed (a flow velocity of up to approximately 100 m/s) dense (solid phase volume fraction > 30%) particle groups composed of large-size propellant particles (particle size of 3–20 mm) in a confined space. At present, research on the mechanism of this erosion phenomenon is rarely reported. In this work, a 3D improved erosion wear model for an FC wall is developed based on the CFD-DEM method introduced in the initial interior ballistic model. Furthermore, erosion wear behavior on the FC is revealed. This study can provide support for a comprehensive understanding of the damage mechanism for an FC in a propulsion system.

2. MODEL FORMULATION

During the initial interior ballistic process, the initial interior ballistic model is used to reproduce the propellant gas source in the chamber. The gas flow is simulated with CFD, and the DEM is employed to capture single particle behavior, thereby improving the accuracy of the erosion wear simulation. The soft sphere model is adopted to indicate the collision details of particles. The wall pseudo-particle model is employed for the collisions between the particle and the surface, and the erosion wear phenomenon is captured by the Oka erosion model. The following simplified assumptions are adopted.

(1) The propellant particles are equivalent to spherical particles with the mass equivalence method.

(2) The diameter reduction caused by the propellant combustion at the initial ballistic stage is considered.

(3) The average diameter of the particle is the equivalent diameter of the particle.

(4) The erosion of the combustion gas on the FC is not considered. Only the mechanical erosion wear of the propellant particles is considered.

2.1 Initial Interior Ballistic Model

During the initial interior ballistic stage, the propellant particles move under the action of the combustion gas. The combustion of the propellant follows the geometric combustion law, which is described as follows.

$$\psi = \chi Z\left(1+\lambda Z+\mu_2 Z^2\right) \tag{1}$$

where ψ and Z represent the percentage and the relative thickness of the burned propellant, respectively. χ, λ, and μ_2 are the shape characteristic parameters of the propellant.

The burning rate of propellant is expressed as follows.

$$\frac{\mathrm{d}Z}{\mathrm{d}t} = \frac{\mu_1}{e_1} P^n \tag{2}$$

where μ_1 is the burning-rate coefficient, e_1 is the arc thickness of the propellant, and P is the average pressure in the chamber.

The state equation of the propellant gas is given as follows.

$$l_\psi = l_0\left[1-\frac{\Delta}{\rho_p}(1-\psi)-\alpha_1\Delta\psi\right] \tag{3}$$

$$\Delta = \frac{m}{V_0} \tag{4}$$

$$l_0 = \frac{V_0}{S_1} \tag{5}$$

where α_1 is the residual volume of the gas and ρ_p is the gunpowder particle density. S_1 is the cross-sectional area of the barrel. m is the mass of the propellant charge. V_0 is the volume of the chamber.

During the initial interior ballistic stage, the projectile's moving equation is expressed as follows.

$$S_1 P = \varphi m_1 \frac{\mathrm{d}v_1}{\mathrm{d}t} \tag{6}$$

Thereinto,

$$v_1 = \frac{\mathrm{d}l}{\mathrm{d}t} \tag{7}$$

$$\varphi = 1+(\frac{\rho}{r})^2\tan^2\theta+(\frac{\rho}{r})^2\upsilon\tan\theta+\frac{1}{3}\frac{m}{m_1}+\frac{m}{M}(1+\frac{m}{m_1}) \tag{8}$$

where φ is the secondary power coefficient. m_1, v_1, l are the mass, the velocity, and the displacement of the projectile. The value of υ is taken as 0.18. ρ and r are the

inertia radius and the radius of the projectile. θ is the rifling angle.

The energy conservation equation during the initial interior ballistic stage is presented as follows.

$$S_1 P\left(l_\psi + l\right) = fm\psi - \frac{\varphi}{2}\left(k_1 - 1\right)mv_1^2 \tag{9}$$

where f is the gunpowder force. k_1 is the adiabatic index. V_0 is the chamber volume.

$$p_\mathrm{d} = P\frac{\varphi_1}{\varphi} \tag{10}$$

$$p_\mathrm{t} = p_\mathrm{d}\frac{\varphi_\mathrm{t}}{\varphi_1} \tag{11}$$

In this work, the projectile base pressure p_d and the chamber bottom pressure p_t are obtained from the initial interior ballistic program. These pressures are utilized as the driving conditions of the particles in the computational model to better reproduce the particle motion in the propulsion system.

2.2 Governing Equations

The two-phase flow in the propulsion system is simulated based on the Eulerian-Lagrangian method. The gas phase follows the Navier-Stokes equations under the Eulerian frame.

$$\frac{\partial\left(\varepsilon_l\rho_l\right)}{\partial t} + \nabla\cdot\left(\rho_l\varepsilon_l\boldsymbol{v}_l\right) = 0 \tag{12}$$

$$\frac{\partial\left(\varepsilon_l\rho_l\boldsymbol{v}_l\right)}{\partial t} + \nabla\cdot\left(\rho_l\varepsilon_l\boldsymbol{v}_l\boldsymbol{v}_l\right) = -\varepsilon_l\nabla p_l + \varepsilon_l\nabla\cdot\boldsymbol{\tau} + \varepsilon_l\rho_l\boldsymbol{g} - \boldsymbol{S} \tag{13}$$

where ε_l, ρ_l, $\boldsymbol{v}_l$, and $\boldsymbol{\tau}$ represent the volume fraction, the density, the velocity, and the viscous stress tensor of the fluid. $\boldsymbol{S}$ is the momentum source term.

In this work, the realizable k-ε model (Shih et al., 1995) is employed to calculate the turbulence. This model is well suited for the working conditions of the gas-solid flow during the initial interior ballistic stage.

$$\frac{\partial}{\partial t}(\rho_l k) + \frac{\partial}{\partial x_i}(\rho_l k u_i) = \frac{\partial}{\partial x_j}\left[\left(\mu + \frac{\mu_t}{\sigma_k}\right)\frac{\partial k}{\partial x_j}\right] + G_k + G_b - \rho_l\varepsilon - Y_M + S_k \tag{14}$$

$$\frac{\partial}{\partial t}(\rho_l\varepsilon) + \frac{\partial}{\partial x_i}(\rho_l\varepsilon u_i) = \frac{\partial}{\partial x_j}\left[\left(\mu + \frac{\mu_t}{\sigma_\varepsilon}\right)\frac{\partial\varepsilon}{\partial x_j}\right] + \rho_l C_1 S\varepsilon - \rho_l C_2\frac{\varepsilon^2}{k+\sqrt{\gamma\varepsilon}} + C_{1\varepsilon}\frac{\varepsilon}{k}C_{3\varepsilon}G_b + S_\varepsilon \tag{15}$$

where k is the turbulent kinetic energy. μ is the dynamic viscosity. γ is the kinematic viscosity. G_k is the generation of turbulent kinetic energy resulting from the velocity gradient. G_b is the generation of turbulent kinetic energy due to the buoyancy. Y_M is the pulsation expansion in compressible turbulence. The constants C_2、$C_{1\varepsilon}$ are set to 1.9 and 1.44, respectively. S_k and S_ε are other source terms. σ_k and σ_ε are taken as 1.0 and 1.2, respectively.

The motion of particles is governed by the Newton dynamic equations within the Lagrangian frame.

$$m_p\frac{\mathrm{d}\boldsymbol{v}_p}{\mathrm{d}t} = \boldsymbol{F}_g + \boldsymbol{F}_I + \boldsymbol{F}_\mathrm{c} + \boldsymbol{F}_p \tag{16}$$

$$2/5\,m_p R^2\frac{\mathrm{d}\boldsymbol{\omega}_p}{\mathrm{d}t} = \boldsymbol{R}_i^*\times\boldsymbol{F}_{\tau,\mathrm{c}} \tag{17}$$

where m_p, $\boldsymbol{v}_p$, $\boldsymbol{\omega}_p$, and $\boldsymbol{F}_g$ represent the mass, the velocity, the angular velocity , and the gravity force of particles. $\boldsymbol{F}_I$ is the drag force, $\boldsymbol{F}_c$ is the collision force, and $\boldsymbol{F}_p$ is the pressure gradient force. $\boldsymbol{R}_i^*$ is the vector from the particle center of mass to the contact point. The subscript τ represents the tangential component force.

In this work, the relative velocity between the gas and particles, as well as the Reynolds number, are large. Therefore, Gibilaro and Gidaspow's drag model (Papadikis et al., 2010; Chen & Yu, 2024) for a high Reynolds number is employed to calculate the drag force.

2.3 Collision and Erosion Model

During the motion of the dense particle group, numerous collisions occur between particles. In this work, the Hertz-Mindlin contact model (Hou et al., 2011; Yang et al., 2014) is employed to consider particle-particle collisions. In this model, the tangential force is constrained by the static friction force. The expressions are presented as follows.

$$\boldsymbol{F}_\mathrm{c} = \boldsymbol{F}_{n,\mathrm{c}} + \boldsymbol{F}_{\tau,\mathrm{c}} \tag{18}$$

$$\boldsymbol{F}_{n,\mathrm{c}} = \frac{4}{3}E^*\sqrt{R^*}\delta_n^{\frac{3}{2}} - 2\sqrt{\frac{5}{6}}\beta_1\sqrt{S_n m^*}\boldsymbol{v}_n^{\overline{rel}} \tag{19}$$

$$\boldsymbol{F}_{\tau,\mathrm{c}} = \min\left\{-S_t\delta_t - 2\sqrt{\frac{5}{6}}\beta_1\sqrt{S_t m^*}\boldsymbol{v}_t^{\overline{rel}}, \mu_s\boldsymbol{F}_{n,\mathrm{c}}\right\} \tag{20}$$

where E^* is the equivalent Young's modulus, R^* is the equivalent radius, S_n is the normal stiffness, S_t is the tangential stiffness, and m^* is the equivalent mass.

Furthermore, numerous collisions take place between particles and the wall. The wall pseudo-particle model is employed to consider the collisions between the particle and the surface. In this model, the wall is regarded as a particle with an infinite mass and an infinite radius. In addition, the normal direction of the collision is the outer normal direction of the surface.

Under the influence of particle collisions, erosion wear occurs on the inner surface of the FC. The Oka erosion model is applicable for pipeline erosion induced by large-size particles (Oka & Yoshida, 2005; Oka et al., 2005). During the IIBP, the particle size is large, and the change of the propellant particle size is little. This conforms to the applicable conditions of the above model. Therefore, the Oka erosion model is employed in this work.

$$H = g(\alpha)E(\alpha)m_p / A \tag{21}$$

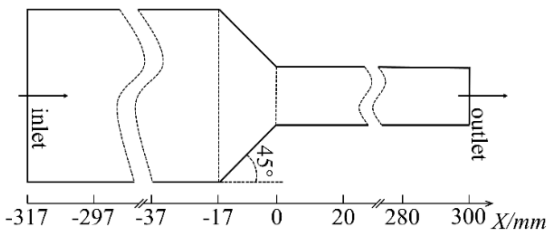

(a) Diagram of the erosion experiment

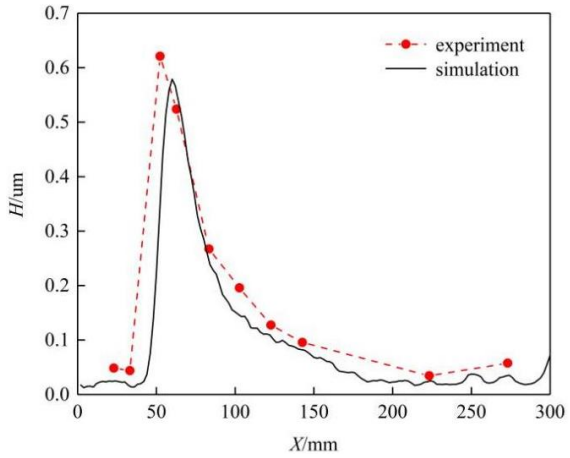

(b) Comparison between simulation and experiment

Fig. 1 The model validation

$$g(\alpha)=\sin(\alpha)^{0.71H_v^{0.14}}\times\left(1+H_v(1-\sin(\alpha))^{2.4H_v^{-0.94}}\right) \tag{22}$$

$$E(\alpha)=65W^{-k_1}\left(\frac{v}{104}\right)^{2.3H_v^{0.038}}\left(\frac{d}{0.326}\right)^{0.19} \tag{23}$$

where H is the erosion depth, A is the area of a triangular element on the wall, and α is the impact angle of the particle. The Vickers hardness of the worn material H_v is taken as 4GPa. The wear constant of the material W is 3 and the empirical coefficient k_1 is -0.12 (Wang et al., 2003; Oka & Yoshida, 2005). v is the particle's impact velocity and d is the particle's diameter when the particle impacts with the surface.

2.4 Model Validation

In this work, the erosion wear experiment reported by Huser & Kvernvold (1998) is used to validate the model, which situation is similar to that of the FC collided by propellant particles. The diagram of the erosion experiment is shown in Fig. 1(a). In this experiment, the diameter of the inlet side is 54 mm, the diameter of the outlet side is 20mm, and the taper angle is 45 °. The diameter of particles in the gas-solid flow is 0.25 mm.

According to the experimental conditions, a numerical simulation was carried out using the above model to obtain the axial distribution of the erosion depth. The comparison between the simulated results and the experimental data is illustrated in Fig. 1(b). The average error is 9.52%. The maximum erosion depth in the simulation occurs at X = 60 mm. This value lies within the range of the experimental maximum erosion depth, which spans from X = 42 mm to X = 63 mm. The

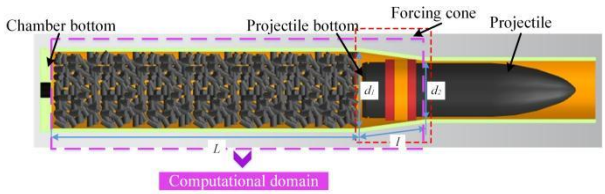

(a) Calculation model of the propulsion system.

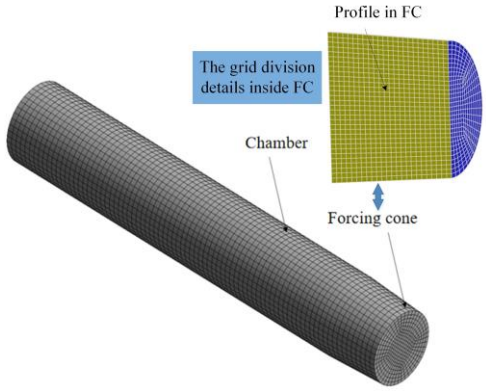

(b) Structural grid division of the computational domain

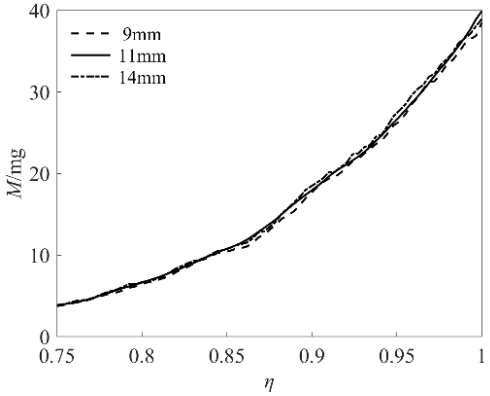

(c) Erosion loss mass simulated by three grid sizes

Fig. 2 The grid division and grid independence verification

simulation results are in agreement with the erosion test data, indicating the reasonable accuracy of this model in predicting the erosion of reducing pipe caused by propellant particles.

3. CALCULATION MODEL

In this work, the erosion wear behavior of the FC caused by propellant particles during the IIBP of the propulsion system was calculated. For the calculation, a 3D coordinate system was established, as illustrated in Fig. 2(a), with the center of the interface between the chamber and the FC as the origin, and the central axis of the barrel defined as the X-axis.

The length of the chamber L, the length of the FC l, the diameter of the chamber d_1, and the diameter of the barrel d_2 are 700 mm, 120 mm, 134 mm, and 122 mm, respectively. The FC's taper (K), which is calculated as follows, is 1/10.

$$K=\frac{d_1-d_2}{l} \tag{24}$$

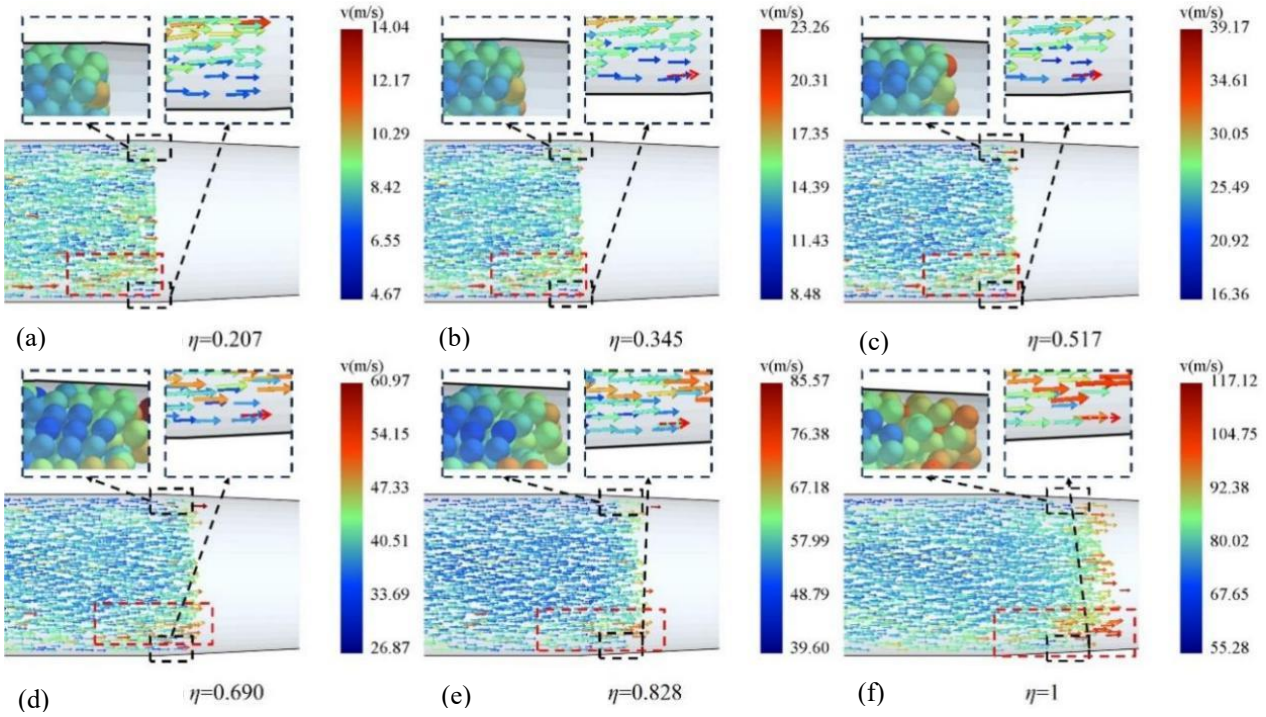

Fig. 3 The particle velocity vector diagram in the FC

Considering the initial ballistic time varies with different charging conditions, the relative time in the initial interior ballistic stage (η) is introduced as Eq. (25) to analyze the erosion wear.

$$\eta = \frac{t}{t_m} \tag{25}$$

The calculation domain is divided by the structural grid, as presented in Fig. 2(b). The changes in the erosion loss mass (M) were monitored for three different grid sizes: 9mm, 11mm, and 14mm, as illustrated in Fig. 2(c). Compared to the simulated results obtained with the 11mm grid size, the average errors in the mass loss of the FC for the 9mm and 14mm grid sizes were 2.02% and 2.83%, respectively. Balancing computational efficiency and accuracy, the grid size of 11mm was selected for subsequent calculations.

4. DISCUSSION OF RESULTS

4.1 The Erosion Wear Behavior on the FC

During the initial ballistic process, the mass equivalent method is adopted to approximate the propellant particles as spherical, considering that the particles burn less. For the condition where K is 1/10 and the charging propellant mass is 6.847 kg, the volume fraction of the particles is 41%. The parameters used in the initial interior ballistic model are illustrated in Table 1. Through the interior ballistic program, the initial ballistic time (t_m) is calculated to be 5.38 ms. The pressures Through the chamber bottom and the projectile bottom are obtained.

Under the action of the combustion gas, the motion of the propellant particle during the initial ballistic stage is shown in Fig. 3. From Fig. 3, the movement direction

Table 1 Parameters used in the initial interior ballistic model

Parameters	Value
Diameter of the barrel (d_2) /mm	122
Volume of chamber (V_0) /L	9.898
Density of the FC wall (ρ_w) /kg·m3	7890
Poisson ratio of the FC wall (μ_F)	0.3
Average equivalent diameter of particles (d) /mm	8.6
Density of particles (ρ_p) /kg·m3	1680
Young's modulus of particles (E_p) /GPa	5.029
Poisson ratio of particles (μ_P)	0.29

of boundary particles is parallel to the chamber wall at η=0.207. At η=0.345, the motion directions of a portion of the front boundary flow particles deviate towards the radial center of the FC due to impacting the FC. The motion direction of particles in the rear is also deflected towards the radial center under the combined action of the obstruction from particles in the front boundary flow and the push from other particles and gas. At η=0.517, the velocity of particles in the transition zone between the core flow and the boundary flow increases as a result of the collision effect of boundary flow particles and the gas phase force. At η=0.690, the particles that move towards the radial center after impacting the FC start to move parallel to the FC wall under the bi-directional action of the core flow particles and the FC wall. Some core flow particles continue to accelerate and overtake the boundary particle flow. At η=0.828, particles at the front of the boundary flow move parallel with the FC wall. At η=1, some particles in the transition zone between the core flow and boundary flow move to the front of the particle group, forming a gushing phenomenon, as shown in Fig. 3(f).

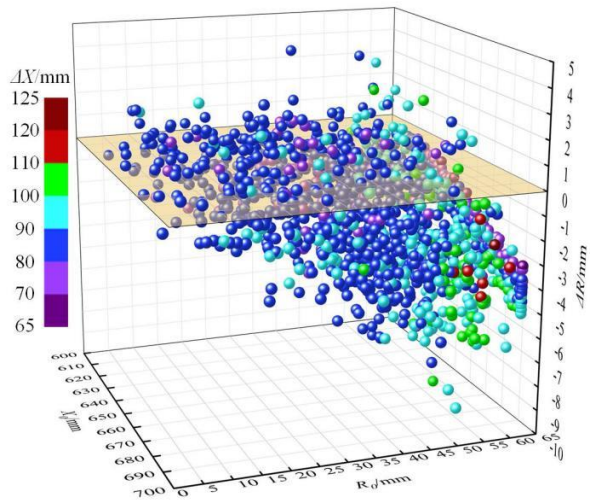

Fig. 4 Axial and radial displacement of particles moving to the FC

To further analyze the mechanism of erosion wear, the particles in the FC at η=1 are taken as the research object to analyze the motion behavior of particles entering the FC. The initial position (X_0, R_0) and axial and radial displacement (ΔX, ΔR) of these particles during IIBP are shown in Fig. 4. As shown in Fig.4, the radial displacement of core flow particles (R_0=0 to R_0=30 mm) is small, while that of boundary flow particles and particles in the transition zone between boundary flow and core flow (R_0=30mm to R_0=65mm) is large. The radial displacement of particles exhibits a positive correlation with the proximity of its initial radial position to the wall. This is because the motion of particles near the wall is subject to a more pronounced influence from the FC wall. Among them, there are three particles with ΔR<-8 mm, particle A_R (X_0=634.1 mm, R_0=62.7 mm), particle B_R (X_0=666.6 mm, R_0=55.3 mm), particle C_R (X_0=695.7 mm, R_0=50.8 mm), which mostly occur in boundary flow and transition zones. There are three particles with ΔR>3 mm, particle E_R (X_0=624.3 mm, R_0=51.1 mm), particle F_R (X_0=634.2 mm, R_0=35.1 mm), particle G_R (X_0=669.0 mm, R_0=22.2 mm), distributed in the transition zone and core flow. The axial displacement of the majority of particles falls within the range of 70 mm to 100 mm, whereas merely a fraction of particles exhibit an axial displacement surpassing 100mm. These particles are initially mainly distributed in the near-wall and sub-near-wall regions. There are seven particles with an axial displacement exceeding 110 mm, which are particle A_x (X_0=695.7 mm, R_0=49.6 mm), particle B_x (X_0=695.7 mm, R_0=52.2 mm), particle C_x(X_0=695.7 mm, R_0=54.9 mm), particle D_x (X_0= 695.7 mm, R_0= 55.1 mm), particle E_x (X_0= 689.6 mm, R_0= 56.2 mm), particle F_x (X_0= 695.7 mm, R_0= 57.1 mm), particle G_x (X_0= 695.7 mm, R_0= 60.1 mm).

For seven particles with a displacement in the axial direction (ΔX) greater than 110 mm, they mainly move under drag and pressure gradient forces, which are the gas-phase forces $F_f = F_I + F_p$. For particles with a displacement in the radial direction (ΔR) less than -8 mm or greater than 3 mm, the significant changes in the radial

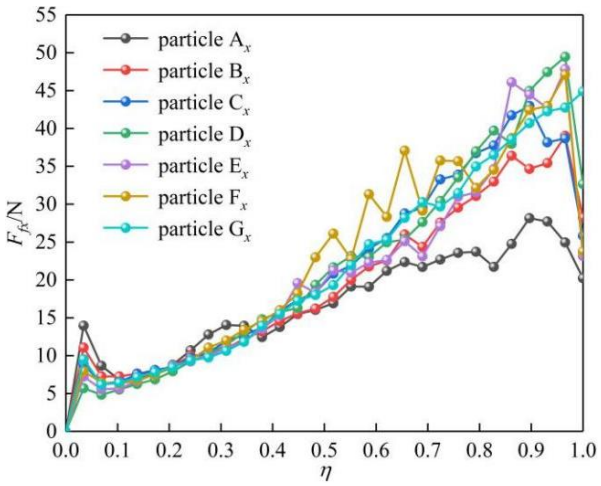

(a) Axial gas-phase force

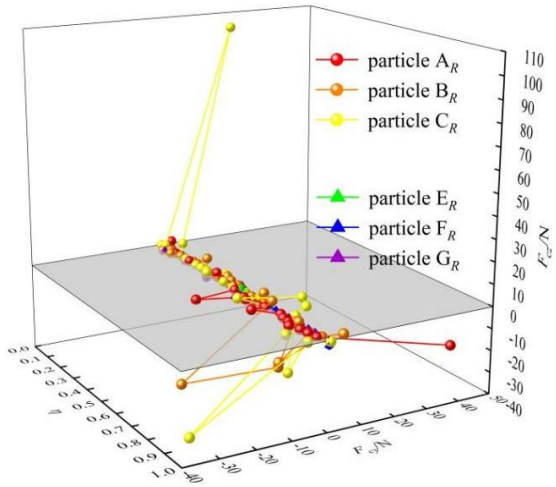

(b) Radial collision force

Fig. 5 Force of characteristic particles

motion of particles are mainly caused by collision. The axial gas force (F_{fx}) of particles with ΔX greater than 110 mm and the radial collision forces (F_{cy} and F_{cz}) of particles with ΔR less than -8 mm or greater than 3 mm, are presented in Fig.5. From Fig. 5(a), the gas-phase force exerted on the particles increases continuously over time. Before η=0.4, particles located far from the wall experience a greater gas-phase drag, while particles located closer to the wall experience greater gas-phase drag after η=0.4. This leads to a continuous and significant augmentation in the acceleration of particles near the wall. In contrast, for particles distant from the wall, the pattern of acceleration increases first ascends and subsequently descends. This is one of the reasons for the formation of the particle gushing phenomenon. From Fig. 5(b), particles in close proximity to the wall are prone to collisions, which have collided with the wall, resulting in a significant collision force. This results in a substantial instantaneous change in the radial velocity and a large radial displacement. However, the particles far away from the wall are subjected to small collision force, and this part of the particles produces radial displacement under the joint action of collision force and gas-phase force.

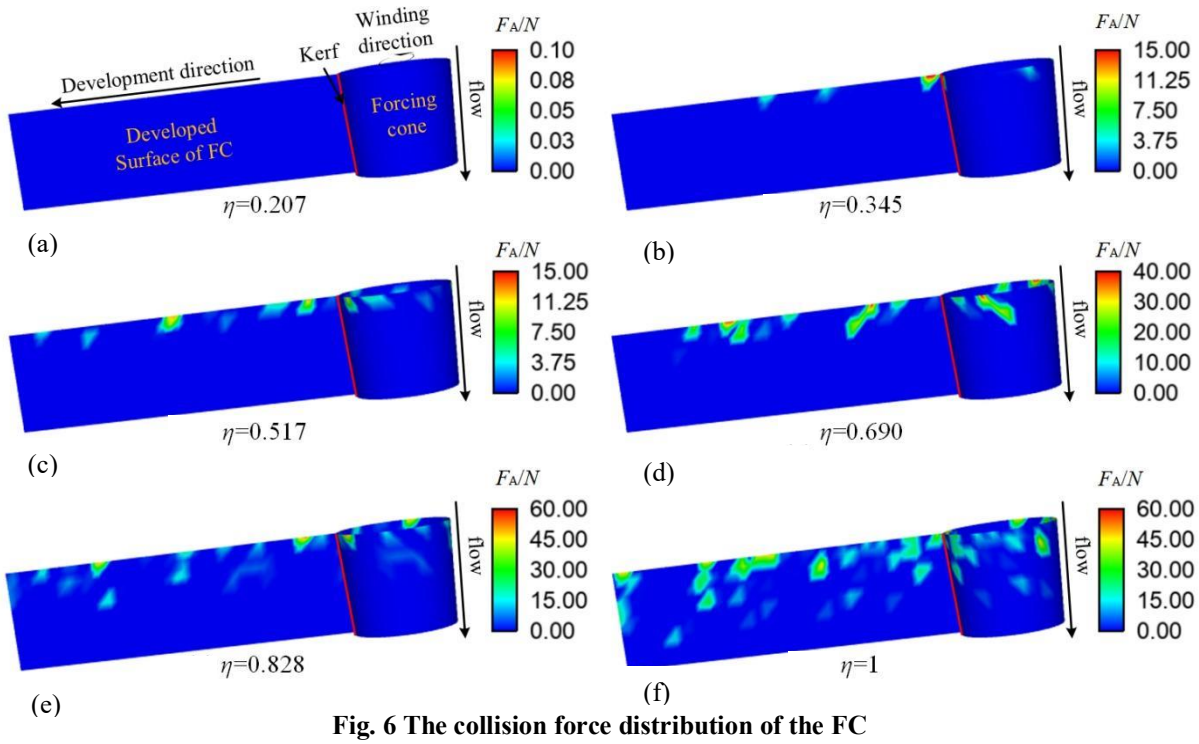

Fig. 6 The collision force distribution of the FC

The distribution of the particle collision force (F_A) on the FC wall during the initial interior ballistics process is shown in Fig. 6. To facilitate the observation of the collision force distribution, the FC is cut along the kerf and unfolded in the development direction to obtain a developed surface. This developed surface can be rewound along the winding direction to obtain the FC again. From the figure, particles have not yet collided with the FC at η=0.207. At η=0.345, the front particles enter the FC region, and some particles collide with the large-diameter side wall of the FC, as shown in Fig. 6 (b). The area where the FC wall collides with particles expands over time. During the period of η=0.345 to η=0.517, the collision area mainly expands in the development direction. During the period of η=0.517 to η=1, the collision area not only expands in the development direction but also expands along the flow direction. The particle collision force on the FC increases continuously over time, which has a significant impact on the erosion wear phenomenon.

Among them, the average normal component of the collision force (average impact force F_N), the average tangential component of that (average friction force F_T), the collision number (n_c) between particles and the FC wall, and the collision angle (α) are shown in Fig. 7. From Fig. 7(a), no collisions between the propellant particles and the FC before η=0.228. As the particle group continues to move to the right, the number of particles colliding with the FC wall rises. Correspondingly, both the average impact force and average friction force significantly increase. During this process, the impact force on the FC wall is greater than the friction force. From Fig. 7(b), the collision angle (α) is distributed in the range of 11 ° to 21 °. With the increase of η, the number of particles impacting the FC (n_c) increases, while the collision angle (α) decreases. It

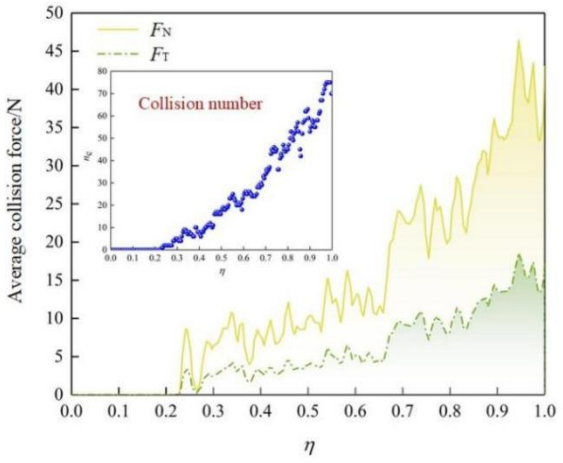

(a) Average collision force (F_N and F_T)

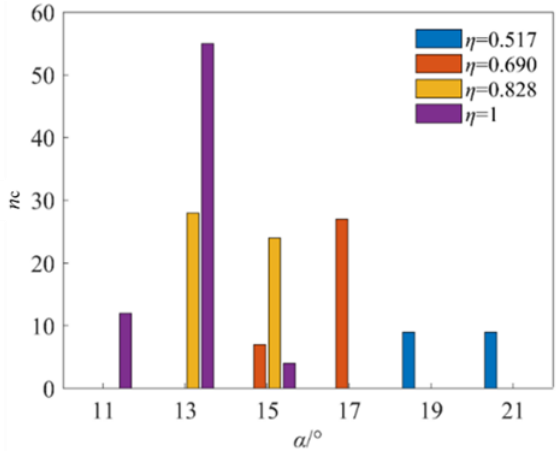

(b) Collision angle of particles

Fig. 7 Collision distribution of particles when K = 1/10

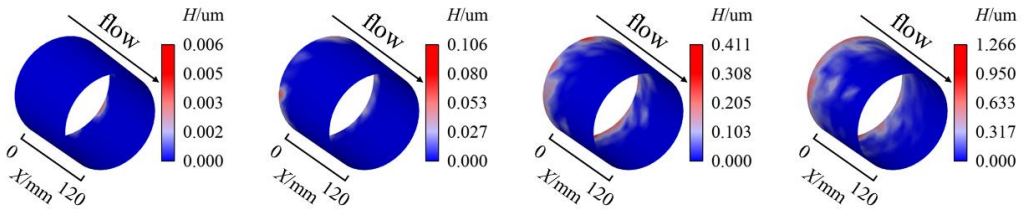

(a) η =0.286 (b) η =0.621 (c) η =0.828 (d) η =1

Fig. 8 Erosion pattern of the FC

indicates that the effect of boundary flow particles on the FC changes from the impact state to the friction state under the bi-directional action of the FC wall and core flow particles.

The erosion distribution on the FC is illustrated in Fig.8. Combined with the preceding figures for analysis, the particles colliding with the FC have low velocity at η=0.621, resulting in a local erosion with a small area at the left end of the FC. At η=0.621, the number of particles colliding with the FC increases. The collision velocity of these particles increases to about 50m/s with a large collision angle. This results in severe erosion on the left end of the FC. After colliding with the FC wall, a portion of the boundary flow particles keep a friction effect on the FC. The erosion amount in the middle of the FC is small under the friction of boundary flow particles and presents a cloud-like distribution at η=0.828. The subsequent boundary flow particles continue to collide with the left end of the FC. The erosion area at the left end of the FC expands and tends to be annular. At η=1, the boundary flow particles at the front end of the particle group collide with the FC in a friction state, resulting in an irregular cloud distribution of the erosion at the middle and right end of the FC with a small erosion amount. The subsequent boundary flow particles collide with the left end of the FC with a certain collision angle, resulting in continuous deterioration of the erosion at the left end of the FC. The erosion on the left end of the FC is obvious, and the distribution is circular.

The distribution of the average erosion depth of the FC along the X-axis is presented in Fig.9. From the Figure, the erosion phenomenon in the left part of the FC is serious. In contrast, the erosion in the middle and right part of the FC is relatively minor. The average erosion depth of the annular sections at the left end of the FC is greater than that at the middle and right ends. This distribution law intensifies over time. The erosion depth of the FC is progressive from left to right, and the X position corresponding to the minimum average erosion depth increases over time.

4.2 The Effect of the FC's Taper on the Erosion Wear of the FC

To investigate the effect of the FC's taper (K) on the erosion wear of the FC, numerical simulations are conducted on erosion wear under conditions for which the FC's tapers (K) are 1/9, 1/8, 1/7, 1/6, and 1/5. The erosion wear of the FC wall is mainly caused by the collisions with particles. The average values of the

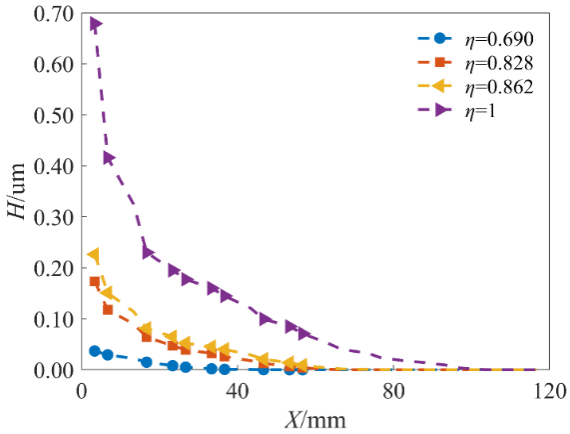

Fig. 9 Average erosion depth of the FC

normal collision force (impact force F_N) and the tangential collision force (friction force F_T) generated by the collision between particles and the FC wall are depicted in Fig. 10, where the FC with different tapers begins to collide with particles successively during the period of η=0.2 to η=0.25. The FC with a taper (K) of 1/5 first begins to collide with the particles, the FCs with K=1/6 to K=1/8 begin to collide with the particles simultaneously, while the FC with a taper (K) of 1/10 begins to collide with particles last. This indicates that the time for the particles to begin to collide with the FC is delayed as the FC's taper increases. In addition, the F_N and F_T acting on the FC wall increase as the taper increases. This is because the angle between the motion direction of the incoming particles and the tangential direction of the FC wall increases as the FC's taper increases, which results in a corresponding increase in the normal impact force of the particles on the FC wall, leading to a significant increase in the sliding friction force between the particles and the FC wall.

The collision number and the average collision angle for different FC tapers are shown in Fig. 11, where the collision numbers for the FCs with different tapers have small differences. The average collision angle of the particles gradually decreases over time. At the same time, the larger the taper of the FC is, the greater the average collision angle is. The collision angle is an important factor that affects erosion wear. According to the erosion models, the two are positively correlated. Consequently, the depth of erosion wear increases with the increase of the collision angle.

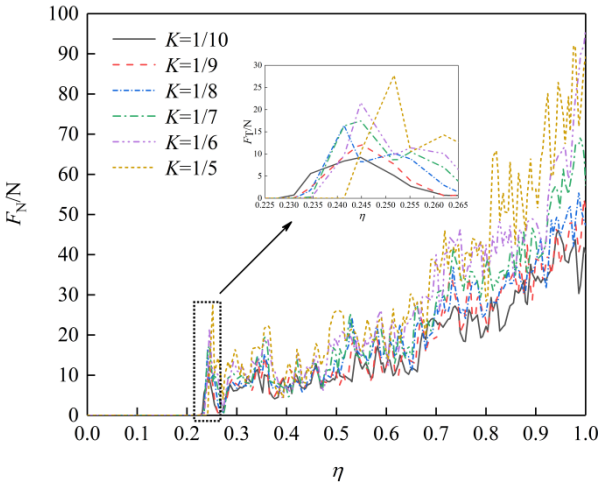

(a) Average collision force

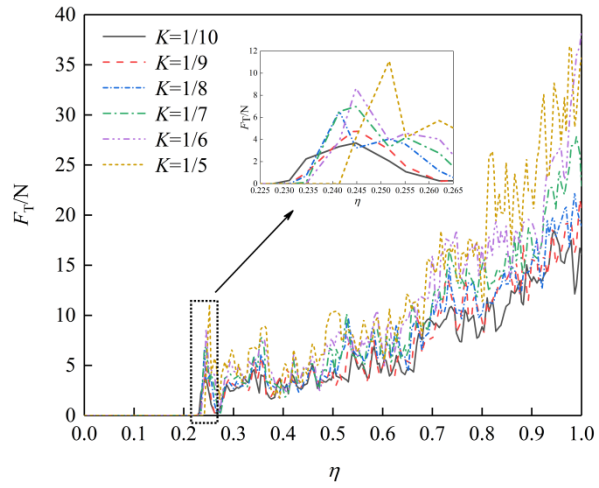

(b) Average friction force

Fig. 10 Change of the average collision force (FN and FT) under different FC's tapers

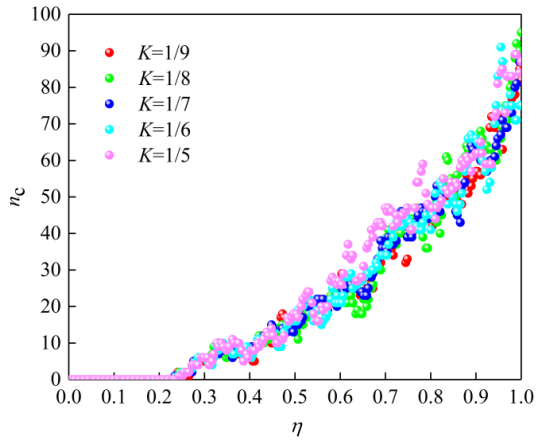

(a) Collision number

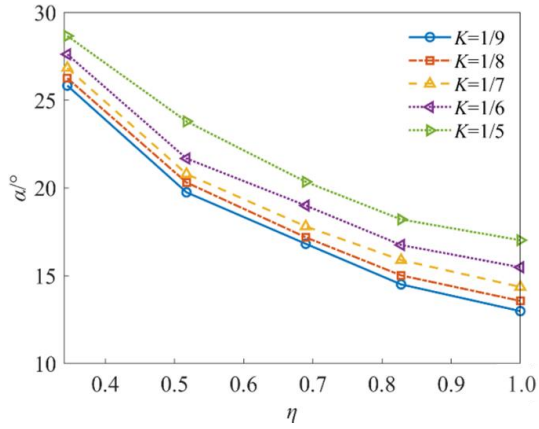

(b) Collision angle

Fig. 11 Changes in average impact angle over time in FC with different taper angles

The distributions of erosion wear on the FC with different tapers are shown in Fig. 12. Figs. 12(a)–12(d), 12(e)–12(h), 12(i)–12(l), 12(m)–12(p), and 12(q)–12(t) represent the distribution of erosion wear on the FC when *K* is 1/9, 1/8, 1/7, 1/6, and 1/5, respectively. Combined with Fig. 8, it can be seen that the maximum erosion wear depth (*H*) increases with the increase of the FC's taper. The erosion wear on the left end of the FC shows a circular distribution, while the erosion wear on the middle and right ends of the FC shows an irregular cloud-like distribution at the end of the IIBP. When η=0.286, a small number of particles enter the FC and begin to collide with it. The left end of the FC is locally worn with a low wear height and a small wear area. When η=0.621, the erosion wear area on the left end of the FC expands, while the wear height is still relatively small. When η=0.828, a large number of particles with high velocity collide with the FC. Some boundary flow particles undergo secondary collisions with the FC, causing the erosion wear on the left end of the FC to increase. The secondary collision area is in the middle of the FC, which increases the erosion wear in this part of the FC. At the same time, the formation of a low-speed zone for boundary flow particles causes wear in the middle of the FC with a large range and a small depth. When η=1, the movement law of the particle group is essentially stable. The erosion wear of the left, middle, and right ends of the FC increases. With the continuous collision of incoming particles, the erosion wear of the left end of the FC forms a circular distribution, and the middle and right ends of the FC form an irregular cloud-like distribution.

To describe the erosion wear distribution of the FC quantitatively, the distributions of the average erosion wear depth of the annular section at different positions of the FC with different tapers are given in Fig. 13, where the erosion wear depth of the left end of the FC is greater than that of the right end of the FC under the same operating conditions. This trend gradually increases with time. The maximum erosion depth significantly increases with the increase of FC's taper. When the FC's taper changes from 1/10 to 1/5, the maximum erosion depth rises by 56.4%. At the same time, the depth of the erosion wear increases with the increase of the FC's taper. This is because of the particle group's movement from left to right. During this process, the front particles of the particle group first collide with the left end of the FC. At this time, the collision angle is large, which causes significant damage to the left end of the FC. In

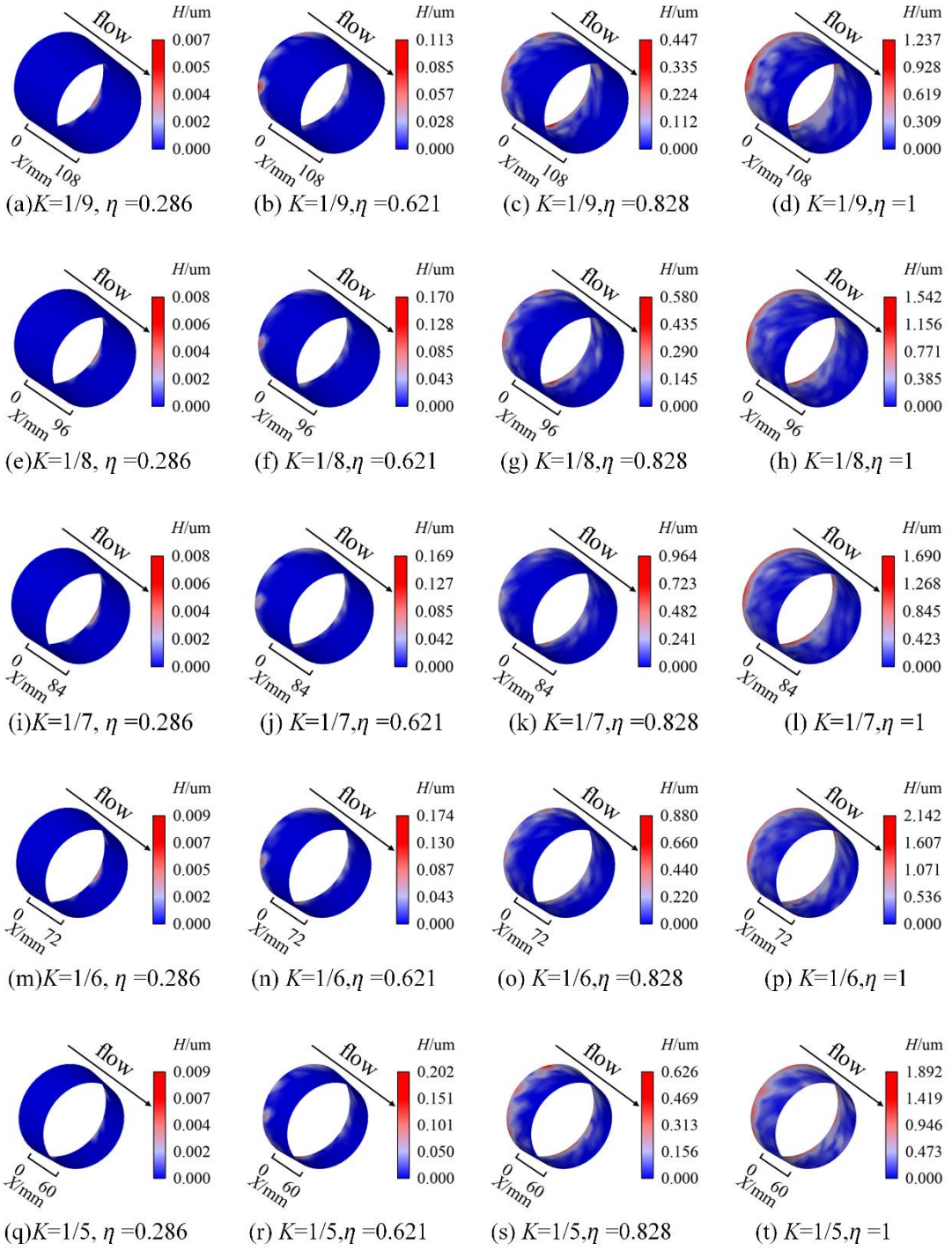

Fig. 12 Erosion wear distribution of FC with different tapers

subsequent movements, the particles in this particle group are in a frictional state with the FC, with a small collision angle and minimal damage to the FC wall. The continuous collision of the particle group with the FC follows this law. The erosion wear of the FC increases as the time increases, thus creating the distribution characteristics.

Figure 14 shows the variation of the overall mass loss of the FC with different tapers over time. The overall mass loss of the FC under various operating conditions is fitted utilizing an exponential equation. The Eq. (26) can be obtained, where M is the overall mass loss of the FC, mg. The fitting parameters (A, B, C) for each operating condition are shown in Table 2.

$$M = AKe^{B\eta} + C \tag{26}$$

According to Fig. 14, the overall mass loss of the FC increases exponentially with time for the same operating conditions. At the same time, the overall mass loss of the FC is positively correlated with the FC's taper. The growth rate of the mass loss ΔM increases with the taper K. When the taper of the FC increases from 1/10 to 1/5, the growth rate of the mass loss ΔM rises by 44.3%, as shown in Table 2. The FC's structure within the propulsion

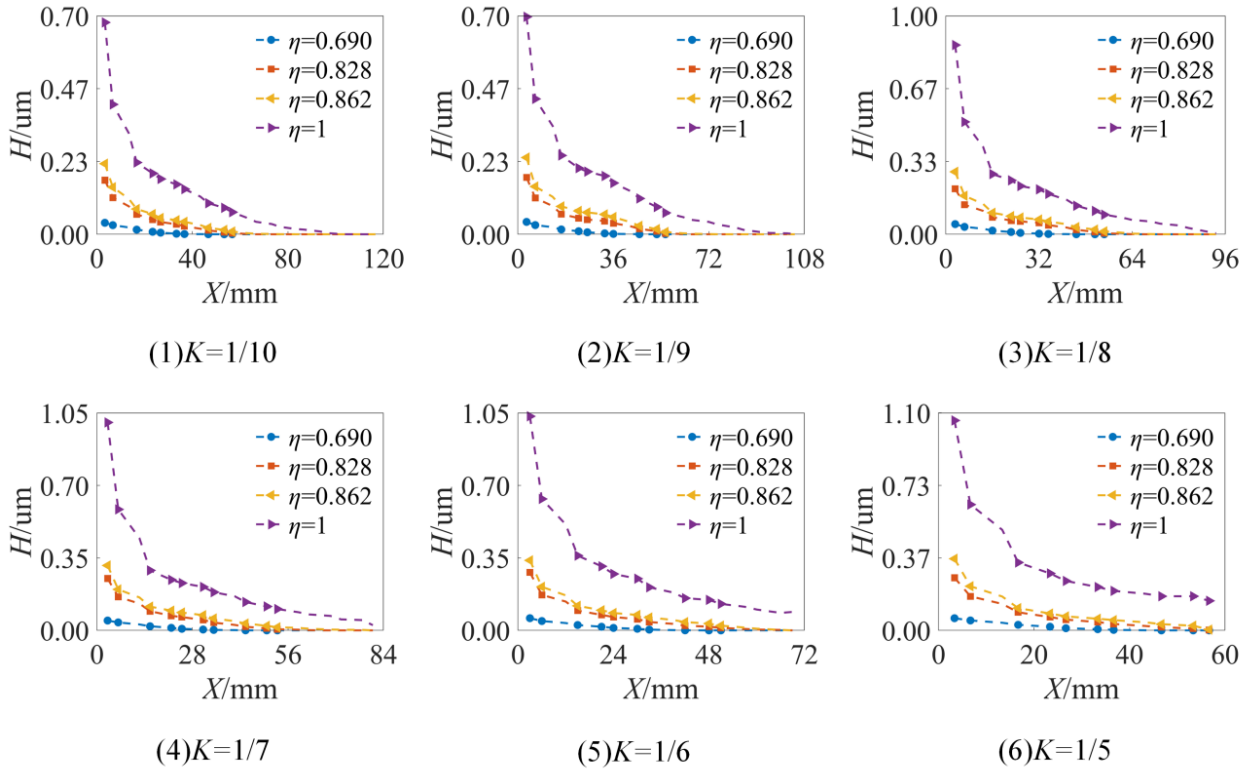

Fig. 13 Distribution of erosion wear depth for FC with different tapers

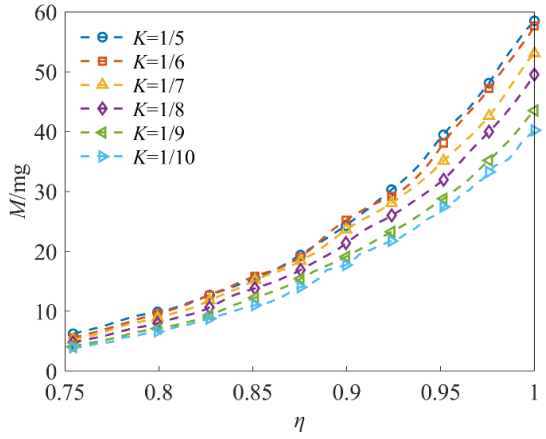

Fig. 14 Change of the erosion loss mass with time under different tapers

Table 2 The fitting parameters under different tapers

K	A / mg	B	C / mg	R^2	ΔM / mg
1/5	0.0374	9.0260	-0.0075	0.9994	52.263
1/6	0.0395	9.0994	-0.0066	0.9966	52.080
1/7	0.0496	8.9407	-0.0071	0.9580	47.811
1/8	0.0468	9.0580	-0.0059	0.9624	44.725
1/9	0.0501	8.9855	-0.0056	0.9625	39.463
1/10	0.0504	9.0182	-0.0050	0.9833	36.224

system can be optimized based on the finding of the impact law of the FC's taper angle on erosion wear characteristics.

5. CONCLUSION

In this study, based on the CFD-DEM method that introduces the initial interior ballistic model, the collision and erosion wear model for an FC caused by a high-speed dense particle group is developed. The particle behavior details and the erosion wear characteristics of the FC during the initial interior ballistic process of the propulsion system are explored, and the effect laws of the FC's taper and the propellant charging mass on the erosion are analyzed. The main conclusions are as follows.

(1) During the initial interior ballistic process, the particle velocity of the boundary particle flow is smaller than the particle velocity of the core particle flow with the obstruction from the FC wall. The particles colliding with the FC wall disturb the motion of the core flow particles, forming a particle-gushing phenomenon. The radial displacement of the particles exhibits a positive correlation with the proximity of the initial radial position to the wall. The axial displacement of the majority of particles falls within the range of 70 to 100 mm, whereas merely a fraction of particles exhibit an axial displacement surpassing 100 mm. Initially, these particles are primarily distributed in the near-wall and sub-near-wall regions.

(2) During the initial interior ballistic process, the collision area between the particles and the FC wall mainly increases in the development direction before η=0.517, while that in both the development direction and the flow direction expands after η=0.517. The collision angle of the particles decreases over time,

leading to the action of the boundary flow particles on the FC wall changing from impact to friction. The left end of the FC is seriously eroded, and the erosion is distributed as annular. The erosion depth of the middle and right sides of the FC is small, and the erosion distribution is shaped as irregular clouds. The overall erosion loss mass increases exponentially over time as $M = 0.00504e^{9.0182\eta} - 0.005$.

(3) When the taper of the FC increases, the time for the particles to begin to collide with the FC is delayed, and the F_N and F_T acting on the FC wall noticeably increase. With the continuous collision of incoming particles, the erosion wear on the left end of FC forms an annular distribution, while the middle and right ends form irregular cloud-like distributions. At the same time, the larger the FC's taper is, the greater the average collision angle is, and the larger the erosion wear depth is. The overall mass loss of the FC is positively correlated with the FC's taper. Furthermore, the overall mass loss of the FC increases exponentially with time. The growth rate of the mass loss increases with the taper K. When the FC's taper changes from 1/10 to 1/5, the maximum erosion depth rises by 56.4%, the growth rate of the mass loss ΔM rises by 44.3%.

ACKNOWLEDGEMENTS

The authors would like to express their gratitude for the financial supports by the Jiangsu Funding Program for Excellent Postdoctoral Talent and the Postdoctoral Fellowship Program of China Postdoctoral Science Foundation (Grant No. GZC20233495).

CONFLICT OF INTEREST

The authors declare that they have no known competing financial interests or personal relationships that could have appeared to influence the work reported in this paper.

AUTHORS CONTRIBUTION

A. Chen: Writing-Original draft preparation, Conceptualization, Software, Validation. **Y. G. Yu:** Visualization, Supervision, Writing-Reviewing and Editing. **S. Xiao:** Methodology, Software.

REFERENCES

Bai, X., Yao, Y., Han, Z., Zhang, J., & Zhang, S. (2020). Study of solid particle erosion on helicopter rotor blades surfaces. *Applied Sciences, 10*, 977. https://doi.org/10.3390/app10030977

Borges, M. F., Antunes, F. V., Prates, P. A., & Branco, R. (2020) A numerical study of the effect of isotropic hardening parameters on mode I fatigue crack growth. *Metals, 10*(2), 177. https://doi.org/10.3390/met10020177

Chen, A. & Yu, Y. (2024). Three-dimensional particle-scale investigation of transient gas–solid flow characteristics in the propulsion system with a complex charge structure. *Physics of Fluids, 36*, 085122. https://doi.org/10.1063/5.0216737

Chen, M. & Tan, L. (2024). Role of particle motion on pressure fluctuation and erosion for a centrifugal pump in energy storage pump station. *Journal of Energy Storage, 99*, 113252. https://doi.org/10.1016/j.est.2024.113252

Chevalier, O., Langlet, A., Fouche-Sanseigne, L., & Guilmard Y. (2015). Assessment of the lifetime of gun barrels under high-speed moving loads. *Journal of Pressure Vessel Technology - Transactions of the ASME, 137*, 015001. https://doi.org/10.1115/1.4027306

Chung, D., Shin, N., Oh, M., Yoo, S., & Nam, S. (2007). Prediction of erosion from heat transfer measurements of 40 mm gun tubes. *Wear, 263*, 246-250. https://doi.org/10.1016/j.wear.2006.12.065

Dhiman, P., Bhat, A., & Karn, A. (2025). Multiphase flow simulations to explore novel technique of air injection to mitigate silt erosion in hydro turbines. *Journal of Applied Fluid Mechanics, 18*(2), 468-484. https://doi.org/10.47176/jafm.18.2.2735

Dou, C., Su, B., Wang, C., Jin, P., Chen, J., Huang, J., & Zhang, C. (2022). A comparative study on gunpowder erosion and promoted ignition combustion of 30SiMn2MoV gun barrel. *Engineering Failure Analysis, 142*, 106741. https://doi.org/10.1016/j.engfailanal.2022.106741

Ewing, M. E., Laker, T. S., & Walker, D. T. (2013). Numerical modeling of ablation heat transfer. *Journal of Thermophysics and Heat Transfer, 27*(4), 615-632. https://doi.org/10.2514/1.T4164

Fu, X., Li, E., & Gao, W. (2009, August 18 - September 20). *Texture feature analysis on erosion and wear in artillery chamber*. 5th International Conference on Information Assurance and Security, Xi'an, Shanxi Province, China. https://doi.org/10.1109/IAS.2009.164

Guo, X., Zang, F., Zhu, Y., & Cao, D. (2025). Aircraft propeller erosion wear and aerodynamic characteristics. *Acta Mechanica Sinica, 41*, 524251. https://doi.org/10.1007/s10409-024-24251-x

Hong, B., Li, Y., Li, Y., Gong, J., Yu, Y., Huang, A., & Li, X. (2023). Numerical simulation of solid particle erosion in the gas-liquid flow of key pipe fittings in shale gas fields. *Case Studies in Thermal Engineering, 42*, 102742. https://doi.org/10.1016/j.csite.2023.102742

Hou, Q., Zhou, Z., & Yu, A. (2011). Computational study of heat transfer in a bubbling fluidized bed with a horizontal tube. *AICHE Journal, 58*(5), 1422-1434. https://doi.org/10.1002/aic.12700

Huser, A. & Kvernvold, O. (1998). *Prediction of sand erosion in process and pipe components*. 1st North American Conference on Multiphase Technology. Banff, Canada, 217-228.

Lee, H., Yang, Y., Chang, W., & Wu, T. (2009). Estimation of heat flux and thermal stresses in multilayer gun barrel with thermal contact resistance. *Applied Mathematics and Computation, 209*, 211-221. https://doi.org/10.1016/j.amc.2008.12.038

Li, S., Wang, L., & Yang, G. (2023a). Surface damage evolution of artillery barrel under high-temperature erosion and high-speed impact. *Case Studies in Thermal Engineering, 42*, 102762. https://doi.org/10.1016/j.csite.2023.102762

Li, S., Wang, L., Xu, F., & Yang, G. (2023b). Numerical simulations for artillery barrel temperature variation considering mechanical friction heat under continuous shots. *International Communications in Heat and Mass Transfer, 142*, 106663. https://doi.org/10.1016/j.icheatmasstransfer.2023.106663

Li, X., Mu, L., Zang, Y., & Qin, Q. (2020). Study on performance degradation and failure analysis of machine gun barrel. *Defence Technology, 16*, 362-373. https://doi.org/10.1016/j.dt.2019.05.008

Li, X., Zang, Y., Mu, L., Lian, Y., & Qin, Q. (2020). Erosion analysis of machine gun barrel and lifespan prediction under typical shooting conditions. *Wear, 444-445*, 203177. https://doi.org/10.1016/j.wear.2019.203177

Li, Y., Fu, J., Qian, L., Zhu, M., Cao, J., & Liu, N. (2024). Research on the erosion of gun barrel based on vented vessel tests. *Tribology Transactions, 67*(2), 270-279. https://doi.org/10.1080/10402004.2024.2306297

Lin, Z, Sun, X, Yu, T, Zhang, Y, Li, Y, & Zhu, Z. (2020). Gas-solid two-phase flow and erosion calculation of gate valve based on the CFD-DEM mode. *Powder Technology, 366*, 395-407. https://doi.org/10.1016/j.powtec.2020.02.050

Oka, Y. I., & Yoshida, T. (2005). Practical estimation of erosion damage caused by solid particle impact part 2: Mechanical properties of materials directly associated with erosion damage. *Wear, 259*(1), 102-109. https://doi.org/10.1016/j.wear.2005.01.040.

Oka, Y. I., Okamura, K., & Yoshida, T. (2005). Practical estimation of erosion damage caused by solid particle impact part 1: Effects of impact parameters on a predictive equation. *Wear, 259*(1), 95-101. https://doi.org/10.1016/j.wear.2005.01.039.

Papadikis, K., Gu, S., Fivga, A., & Bridgwater, A. B. (2010). Numerical comparison of the drag models of granular flows applied to the fast pyrolysis biomass. *Energy Fuels, 24*, 2133-2145. https://doi.org/10.1021/ef901497b

Peng, W. & Cao, X. (2016). Numerical prediction of erosion distributions and solid particle trajectories in elbows for gas-solid flow. *Journal of Natural Gas Science and Engineering, 30*, 455-470. https://doi.org/10.1016/j.jngse.2016.02.008

Perera, Q., K.ward, H., Guzzomi, F., & Vafadar, A. (2024). Erosion wear characterization of an open Ductile Iron butterfly valve subjected to Aluminium Oxide particle slurry flow. *Tribology International, 191*, 109199. https://doi.org/10.1016/j.triboint.2023.109199

Rezgui, N., Mickovic, D. M., Zivkovic, S. Z., & Ivanovic, I. B. (2019). Experimental and numerical analysis of thermo-chemical erosion in gun steel. *Thermal Science, 23*(2A), 599-612. https://doi.org/10.2298/TSCI180608194R

Shih, T. H., Liou, W. W., Shabbir, A., Yang, Z., & Zhu, J. (1995). A new k-ϵ eddy viscosity model for high reynolds number turbulent flows. *Computers & Fluids, 24*(3), 227-238. https://doi.org/10.1016/0045-7930(94)00032-T

Singh, V., Kumar, S., & Mohapatra, S. K. (2019). Modeling of erosion wear of sand water slurry flow through bipe Bend using CFD. *Journal of Applied Fluid Mechanics, 12*(3), 679-687. https://doi.org/10.29252/jafm.12.03.29199

Sopok, S., Rickard, C., & Dunn, S. (2005). Thermal-chemical-mechanical gun bore erosion of an advanced artillery system part two: modeling and predictions. *Wear, 258*(1-4), 671-683. https://doi.org/10.1016/j.wear.2004.09.030

Tao, C., Zhang, Y., Li, S., Jia, C., Li, Y., Zhang, X., & He, Z. (2010). Mechanism of interior ballistic peak phenomenon of guns and its effects. *Journal of Applied Mechanics-Transactions of the ASME, 77*(5), 051405. https://doi.org/10.1115/1.4001561

Underwood, J. H., Witherell, M. D., Sopok, S., McNeil, J. C., Mulligan, C. P., & Vigilante, G. N. (2004). Thermomechanical modeling of transient thermal damage in cannon bore materials. *Wear, 257*, 992-998. https://doi.org/10.1016/j.wear.2004.07.008

Wang, C., Liu, M., & Yan, J. (2023). Flow irreversibility versus wear of elbow-reducer connection with gas-solid two-phase flow: A numerical study via CFD-DEM coupling method. *Powder Technology, 428*, 118835. https://doi.org/10.1016/j.powtec.2023.118835

Wang, L., Li, S., Xu, F., & Yang, G. (2022). United computational model for predicting thermochemical-mechanical erosion in artillery barrel considering friction behavior. *Case Studies in Thermal Engineering, 29*, 101726. https://doi.org/10.1016/j.csite.2021.101726

Wang, M., Dong, H., Wang, Q., Li, J., & Zhao, L. (2003). Microstructures and mechanical properties of high strength gun steels. *Ordnance Material Science and Engineering, 26*(002), 7-10. https://doi.org/10.14024/j.cnki.1004-244x.2003.02.002.

Wang, S., Shi, J., Han, X., Zhu, L., Bi, J., Wang, J., Wang, S., Ma, Z., & Wang, Z. (2022). Effect of pipe orientation on erosion of π-shaped pipelines. *Powder Technology, 08*, 117769.

https://doi.org/10.1016/j.powtec.2022.117769

Wang, Y., Pu, C., Luan, Y., Fu, E., Du, J., & Xiao, Z. (2024) Preparation and performance studies on organic-inorganic phase change composites based on zeolitic imidazolate and paraffin for reducing gun barrel erosion. *Journal of Energy Storage 100*, 113457. https://doi.org/10.1016/j.est.2024.113457

Xie, R., Cao, X., Zhang, J., Sun, X., Fu, C., & Wu, C. (2020). Study of erosion behavior in elbows mounted in series using computational fluid dynamics method. J*ournal of Energy Resources Technology-Transactions of the ASME, 142*(11), 113001. https://doi.org/10.1115/1.4047252

Yang, M., & Yu, Y. (2024). Study on interior ballistic characteristics of worn gun considering projectile engraving process. *Journal of Mechanical Science and Technology 38*(12), 6529~6538. https://doi.org/10.1007/s12206-024-1109-6

Yang, S., Luo, K., Fan, J., & Cen, K. (2014). Particle-scale investigation of the solid dispersion and residence properties in a 3-D spout-fluid bed. *AICHE Journal, 60*(8), 2788-2804. https://doi.org/10.1002/aic.14494

Yang, Y., Zhang, X., Xu, C., & Fan, L. X. (2020). Dynamic stress analysis of anisotropic gun barrel under coupled thermo-mechanical loads via finite element method. *Latin American Journal of Solid and Structures, 17*(1), e243. https://doi.org/10.1590/1679-78255800

Zhang, J., Zhang, H., Liu, Y., & Zhang, C. (2021). Erosion wear characteristics of tee tubes with gas-solid two-phase flow. *Journal of Pressure Vessel Technology - Transactions of the ASME*, *143*, 064502. https://doi.org/10.1115/1.4051068

Zolfagharnasab, M. H., Salimi, M., Zolfagharnasab, H., Alimoradi, H., Shams, M., & Aghanajafi, C. (2021). A novel numerical investigation of erosion wear over various 90-degree elbow duct sections. P*owder Technology, 380*, 1-17. https://doi.org/10.1016/j.powtec.2020.11.059

Zou, L., Yu, C., Feng, G., Zhong, J., & Lv, Y. (2020). Establishment of erosion model of gun steel material and study on its erosion performance. *Journal of Mechanical Science Technology, 34*(5), 2019-2026. http://doi.org/10.1007s12206-020-0423-x